Magnetorotational Instability in a Short Couette Flow of Liquid Gallium

Hantao Ji[*], Jeremy Goodman[†], Akira Kageyama[**], Michael Burin[†], Ethan Schartman[*] and Wei Liu[*]

[*]*Princeton Plasma Physics Laboratory, Princeton University, New Jersey, USA*
[†]*Princeton University Observatory, Princeton, New Jersey, USA*
[**]*Earth Simulator Center, Yokohama, Japan*

Abstract. A concise review is given of an experimental project to study magnetorotational instability (MRI) in a short Couette geometry using liquid gallium. Motivated by the astrophysical importance and lack of direct observation of MRI in nature and in the laboratory, a theoretical stability analysis was performed to predict the required experimental parameters. Despite the long-wavelength nature of MRI, local analysis agrees excellently with global eigenmode calculations when periodic boundary conditions are used in the axial direction. To explore the effects of rigidly rotating vertical boundaries (endcaps), a prototype water experiment was conducted using dimensions and rotation rates favored by the above analysis. Significant deviations from the expected Couette flow profiles were found. The cause of the discrepancy was investigated by nonlinear hydrodynamic simulations using realistic boundary conditions. It was found that Ekman circulation driven by the endcaps transports angular momentum and qualitatively modifies the azimuthal flow. Based on this new understanding, a new design was made to incorporate two independently driven rings at each endcap. Simulations were used to optimize the design by minimizing Ekman circulation while remaining within engineering capabilities. The new apparatus, which has been constructed and assembled, is currently being tested with water and will be ready for the MRI experiment with gallium soon. This development process illustrates the value of interplay between experiment, simulation, and analytic insight.

INTRODUCTION

Accretion disks are the most efficient energy source known to astrophysics. Whereas hydrogen fusion has a maximum efficiency for converting rest-mass to radiation of $\sim 1\%$, accretion onto a black hole or neutron star can have an efficiency of $\sim 5 - 40\%$. Accretion disks are thought to power many of the most luminous and violent astrophysical sources, including X-ray binaries, quasars, and perhaps gamma-ray bursts. Protostellar accretion disks, though energetically much less efficient, are nevertheless of great interest as sites of planet formation.

Magnetorotational instability (MRI), although originally discovered by Velikhov [1] and Chandrasekhar [2], did not come to the attention of the astrophysical community until rediscovered by Balbus & Hawley [3] and verified numerically [4, 5, 6]. Now it has become widely accepted that MRI-driven magnetohydrodynamic (MHD) turbulence, or its variations, is the main cause of rapid accretion and fast angular momentum transport in accretion disks that are warm enough to be partially ionized [7]. We note that some astrophysicists argue from laboratory evidence that purely hydrodynamic turbulence can

account for the inferred accretion especially in cold disks [8, 9] (see below).

In ideal MHD, MRI occurs when the radial gradients of angular velocity, Ω, and specific angular momentum, $j = r^2\Omega$, are oppositely directed: $\partial\Omega^2/\partial r < 0$, $\partial j^2/\partial r > 0$. This is the case for most accretion disks, since the angular velocity profile is expected to be close to keplerian, $\Omega \propto r^{-3/2}$. As a fluid element *gains angular momentum*, it migrates to a larger radius and *lower angular velocity*. This produces a runaway instability when two elements are connected by a weak magnetic tension that exchanges angular momentum between them. Stability prevails if the field is too strong to be stretched, or if resistive diffusion straightens the lines faster than the flow distorts them. Typical growth rates are rapid, $\sim \Omega$.

Linear MRI is simple, generic, and robust. However, whereas many of the important hydrodynamic and MHD instabilities of fundamental importance to astrophysics are observed on the Earth (*e.g.* the Rayleigh-Taylor, Kelvin-Helmholtz, and kink instabilities) or perhaps on the Sun (Parker instability), MRI has never been conclusively observed. We have therefore proposed [10, 11] an experimental study of MRI using a magnetized Couette flow: that is, a conducting liquid (gallium) bounded by concentric differentially rotating cylinders and subject to an axial magnetic field. Despite the fact that confinement of the liquid is provided by the outer cylinder rather than by gravity, as in accretion disks, the underlying mechanism and effect of MRI is essentially the same, *viz.* the turbulent outward transport of angular momentum. Magnetized-Couette-flow experiments have been performed [12, 13, 14, 15], but they have not studied the MRI. They studied magnetic modifications of Rayleigh's centrifugal instability, which requires $\partial j^2/\partial r < 0$, a condition not normally satisfied in accretion disks.

This contribution is intended to provide a concise review of the ongoing gallium project, which involves a constant interplay between experiment, simulation, and theory. We begin with a summary of the theoretical analysis, followed by results from our prototype water experiment and hydrodynamic simulations. We describe a new optimized design and apparatus with maximum possible external controls of boundary conditions, followed by a brief discussion of ongoing efforts by other groups.

THEORETICAL STABILITY ANALYSIS

Local analysis of linear stability

Couette flow involves a liquid confined between rotating coaxial cylinders of radii $r_1 < r_2$, height h and angular velocities Ω_1, Ω_2. In a laminar steady state with $h \gg r_2 - r_1$, constancy of the viscously-transported radial angular momentum flux implies

$$\Omega(r) = a + \frac{b}{r^2}, \tag{1}$$

where $a = (\Omega_2 r_2^2 - \Omega_1 r_1^2)/(r_2^2 - r_1^2)$ and $b = r_1^2 r_2^2(\Omega_1 - \Omega_2)/(r_2^2 - r_1^2)$. The Rayleigh stability criterion is $a\Omega > 0$, *i.e.*, specific angular momentum increases with radius. In the magnetized case, an axial background magnetic field $B_0 = Be_z$ is assumed. Dissipation is determined by the kinematic viscosity, ν, and especially magnetic diffusivity, η.
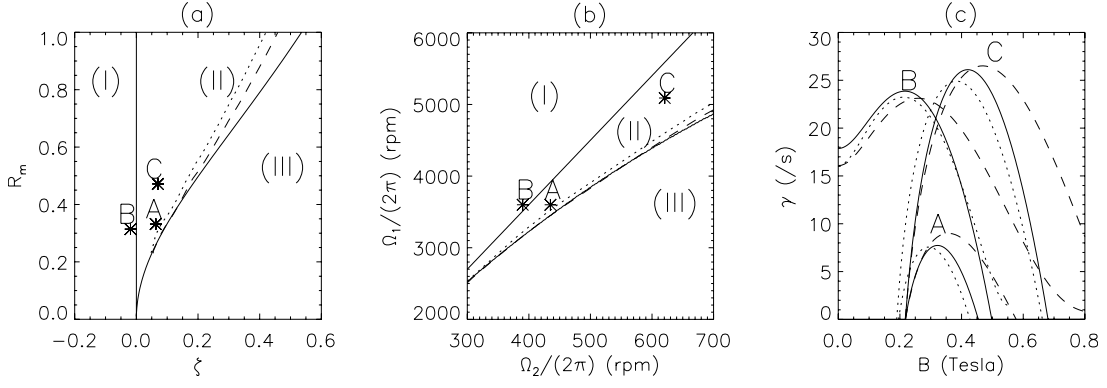
FIGURE 1. (a) Stability of a rotating liquid metal disk in dimensionless parameter space of (R_m, ζ) for the case of $\varepsilon = 1$. Here the stability can be divided into 3 regions: region (I) is hydrodynamically unstable but can be stabilized by a large enough magnetic field, as exemplified by point B. Region (II) is hydrodynamically stable but can be destabilized by presence of a magnetic field (MRI), as exemplified by points A and C. Region (III) is always stable. (b) Stability diagram in Ω_1 and Ω_2 space with dimensions r_1=0.05m, r_2=0.15m, and h =0.1m. The growth rates of points A, B, and C are also shown as functions of magnetic field in (c). Results from global eigenmode analysis are also shown: dotted lines for conducting boundary conditions and dashed lines for insulating boundary conditions.

Comparison with global linear analyses [11, 16, 17, 18, 19] confirms that WKB methods describe the stability of this system very well even on the largest scales. In cylindrical coordinates (r, θ, z) and for axisymmetric perturbations proportional to $\exp(st - ik_z z - ik_r r)$, the WKB dispersion relation is [20, 10]

$$[(s + \nu k^2)(s + \eta k^2) + (k_z V_A)^2]^2 \frac{k^2}{k_z^2} + \kappa^2 (s + \eta k^2)^2 + \frac{\partial \Omega^2}{\partial \ln r}(k_z V_A)^2 = 0, \qquad (2)$$

where the epicyclic frequency $\kappa \equiv (2\zeta)^{1/2}\Omega$ is the maximum frequency of stable oscillations in the unmagnetized case and $V_A \equiv B/\sqrt{\mu_0 \rho}$ (Alfvén speed). We presume that k_z and k_r are nonzero multiples of π/h and $\pi/(r_2 - r_1)$, respectively. The following dimensionless parameters are convenient: aspect ratio $\varepsilon \equiv k_r/k_z$ (reducing to $h/(r_2 - r_1)$ for the fundamental mode), scaled vorticity $\zeta \equiv (r\Omega)^{-1}\partial(r^2\Omega)/\partial r$, magnetic Prandtl number $P_\mathrm{m} \equiv \nu/\eta$, magnetic Reynolds number, $R_\mathrm{m} \equiv \Omega/\eta(k_z^2 + k_r^2)$, and Lundquist number, $S \equiv k_z V_A/\eta(k_z^2 + k_r^2)$. In liquid metals, viscosity is much smaller than resistivity, $P_\mathrm{m} \sim 10^{-6}$. As $P_\mathrm{m} \to 0$, instability occurs when

$$\zeta < \frac{2S^2}{S^2 + 1} - \frac{S^4(1 + \varepsilon^2)}{2R_\mathrm{m}^2(S^2 + 1)}. \qquad (3)$$

The Rayleigh stability criterion $\zeta \geq 0$ follows by taking $S \to 0$ (unmagnetized case).

The stability condition (3) defines a two-dimensional surface in the parameter space (S, ζ, R_m) at fixed ε. Stability boundaries in the (R_m, ζ) plane are shown in Fig. 1(a) for the case of $\varepsilon = 1$. Region (I) is hydrodynamically unstable but can be stabilized

TABLE 1. Parameters for a gallium disk with $r_1 = 0.05$m, $r_2 = 0.15$m, and $h = 0.1$m.

point	$\Omega_1/2\pi$(rpm)	$\Omega_2/2\pi$(rpm)	R_{m}	ζ
A	3600.00	435.00	0.3319	0.06293
B	3600.00	390.00	0.3143	-0.01899
C	5089.77	620.70	0.4715	0.06984

by a finite magnetic field. This region has been extensively studied both theoretically and experimentally [21], and is exemplified by point B. Region (II) is hydrodynamically stable but destabilized by a finite S or magnetic field. Stability returns at even larger S. Stability at $S = 0$ and as $S \to \infty$ are hallmarks of MRI [3, 7]. (In ideal MHD, instability extends formally to $S = 0^+$.) Region (II) has never been studied experimentally. Region (III) is always stable. The boundary between regions (II) and (III) occurs where (3) is an equality and $\partial\zeta/\partial S = 0$:

$$\zeta = 2 - \frac{1+\varepsilon^2}{R_{\mathrm{m}}^2}\left(\sqrt{1 + \frac{4R_{\mathrm{m}}^2}{1+\varepsilon^2}} - 1\right), \qquad S^2 = \sqrt{1 + 4R_{\mathrm{m}}^2/(1+\varepsilon^2)} - 1. \qquad (4)$$

It is useful to project the stability diagram onto experimentally controllable parameters. To apply the local dispersion relation, we take

$$\zeta \;\equiv\; \frac{2(\Omega_2 r_2^2 - \Omega_1 r_1^2)}{\bar\Omega}, \quad \bar\Omega \equiv \sqrt{\Omega_1\Omega_2}, \quad R_{\mathrm{m}} \equiv \frac{h^2\bar\Omega}{\eta\pi^2(1+\varepsilon^2)},$$

and $S \equiv hV_A/\pi\eta(1+\varepsilon^2)$ as above. Figure 1(b) shows stability in the (Ω_1, Ω_2) plane for an annulus of dimensions r_1=0.05m, r_2=0.15m, and h=0.1m (hence $\varepsilon = 1$) filled with gallium ($\rho \simeq 6 \times 10^3$kg/m^3, $\eta \simeq 0.2$m^2/s, $\nu \simeq 3 \times 10^{-7}$m^2/s). Table 1 lists the physical parameters at points A, B, and C. The corresponding growth rates are shown as functions of magnetic field in Fig. 1(c).

Global analysis of linear stability

WKB is a short-wavelength approximation, yet for the experimental parameters contemplated above, the fastest-growing MRI modes are predicted to have wavelengths twice the gap width and cylinder height. It is not clear that the WKB dispersion relation is applicable to these modes, so we have performed a global linear stability analysis [11]. Periodicity in the axial direction simplifies the governing equation to a tenth-order equation in the r direction:

$$\left\{\left[(s - \nu D_k)(s - \eta D_k) + (k_z V_A)^2\right]\frac{1}{2\Omega}\left[(s - \nu D_k)(s - \eta D_k) + (k_z V_A)^2\right](-k_z^{-2}D_k)\right.$$

$$\left. + (s - \eta D_k)\frac{(r^2\Omega)'}{r}(s - \eta D_k)\right\}B_r \;=\; -(k_z V_A)^2 r\Omega' B_r, \qquad (5)$$

where $D_k \equiv \partial^2/\partial r^2 + (1/r)\partial/\partial r - 1/r^2 - k_z^2$. Chandrasekhar [21] performed the first global linear analysis of non-ideal magnetized Couette flow, but he discarded the shear
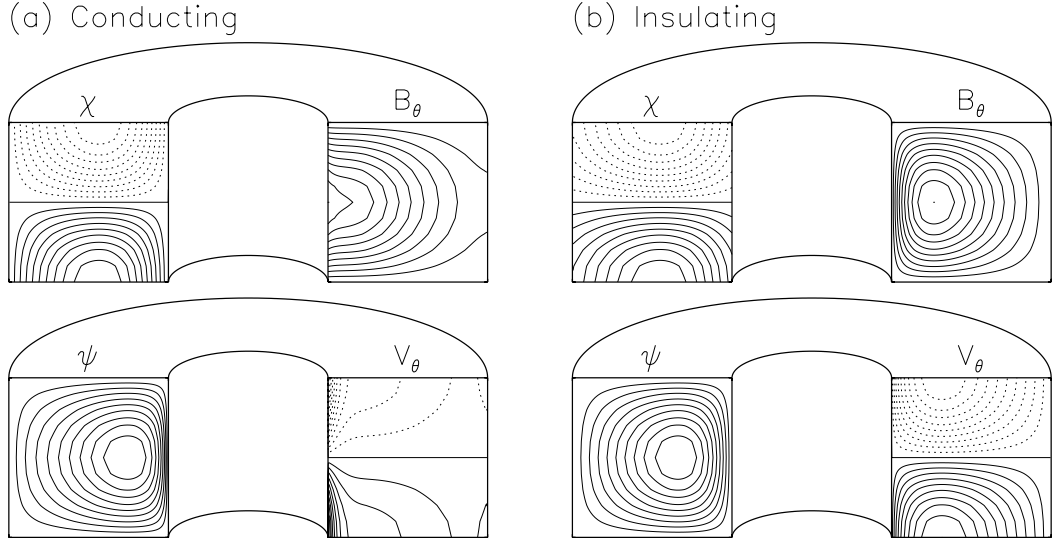
FIGURE 2. Eigenmodes for conditions given by point C in Fig.1 at $B = 0.3$ Tesla with conducting (a) and insulating (b) radial boundaries. Here, solid (dotted) lines represent positive (negative) values; χ and ψ are poloidal flux and stream functions, respectively.

term on the right-side of (5) as appropriate for the Rayleigh unstable cases, as did almost all subsequent work. It was shown that the absence of this shear term eliminates MRI both in the narrow-gap limit [11] and in more general cases [22]. This can be also easily seen in the local dispersion relation (2), where the shear term corresponds to the last term in the left-hand side. Without this term, the first term in the stability condition (3) would be absent, eliminating possibility of MRI.

We have written a linearized, finite-difference, implicit initial-value code to discover the fastest-growing mode. The code deals stably with radial boundary layers and is capable of finding overstabilities: *i.e.*, a growing oscillations with complex eigenfrequency. In fact, all our growing modes turn out to be non-oscillatory. Axisymmetry is assumed, and periodic vertical boundary conditions with periodicity length twice the cylinder height, so that the vertical velocity has nodes at both ends of the cylinder. The equations of motion are discretized on a radial grid. Radial boundaries are impenetrable ($\delta V_r = 0$), no-slip ($\delta V_\theta = \delta V_z = 0$), and electrically either perfectly insulating ($\delta B_\theta = 0$) or perfectly conducting ($\delta B_r = 0$). Results of the global and WKB analyses are compared in Fig. 1. Although the eigenfunctions are very nonsinusoidal, especially in the velocities near the boundaries, the growth rates agree remarkably well with the WKB predictions. Figure 2 shows eigenmodes for the parameters of point C with B=0.3 Tesla. Differences between the conducting and insulating cases can be seen near the inner boundaries. A boundary layer consisting of large toroidal and axial velocities within a radial thickness of $\sim (\nu/\kappa k_z)^{1/3} < 1$mm (not visible in Fig. 2), forms at the inner conducting boundary where the Lorentz force, $\delta j_r \times B_z$, balances the viscous force [11].
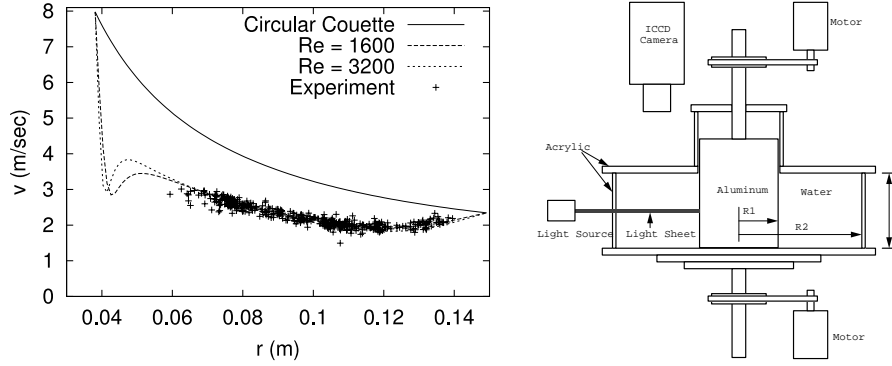
FIGURE 3. Toroidal velocity profiles (left panel) in the hydrodynamic simulations compared to the Couette flow solution and experimental measurements at $z = 4$cm, $\Omega_1/2\pi = 2000$ rpm and $\Omega_2/2\pi = 150$ rpm. Experimental apparatus is shown in the right panel, where $r_1 = 3.8$cm, $r_2 = 14.9$cm, and $h = 10$cm.

PROTOTYPE WATER EXPERIMENT

The periodic vertical boundary conditions assumed above take no account of viscous layers at the top and bottom of the flow. (The top must be capped because of large radial pressure gradients.) The main effect of these viscous boundary layers is to drive Ekman circulation, which flows more rapidly against a weak angular-momentum gradient than against uniform rotation. A simple estimate of the thickness of the Ekman layer $\delta_E \approx \sqrt{\nu/\bar{\Omega}}$ is small ($\sim 10^{-3}h$), and the Ekman circulation time $h/2\sqrt{\nu\bar{\Omega}} \sim 10$ s is much longer than a typical MRI growth time if we use the laminar value for the viscosity ν; turbulent boundary layers may produce much more rapid Ekman circulation.

In order to explore these issues, prototype water experiments were performed in a short circular Couette flow, illustrated in Fig. 3. A container made of transparent acrylic plates and cylinders is mounted on a stainless steel flange which is driven by a DC motor. The speed is measured by a laser-based tachometer. The inner cylinder, made of aluminum, is inserted through a lip seal from the top and is driven in the direction of the container by an AC motor with a controller. The dimensions are $r_1 = 0.038$m, $r_2 = 0.149$m, and $h = 0.1$m.

A PIV technique [23] is used to measure flow profiles as a function of radius and height. Small particles with sizes on the order of 1 μm made of mica and titanium dioxide are mixed in the water. Since the particles are sufficiently small, they couple closely with the water flow. The particles are illuminated by a light sheet with a thickness of about 0.5 cm, which is generated by a horizontal slit in front of a bright halogen light source. An electronically gated intensified-CCD camera records images of illuminated particles at a given height. The images are saved to a PC using a frame-grabber with a rate of 60 images per second. The illuminated particles appear in the images as streaks elongated in proportion to flow speed. By repeating measurements at different radii and heights, toroidal flow can be mapped out as a function of r and z. The measurements were benchmarked at various heights for a case of rigid rotation at $\Omega_1/2\pi = \Omega_2/2\pi = 150$ rpm.
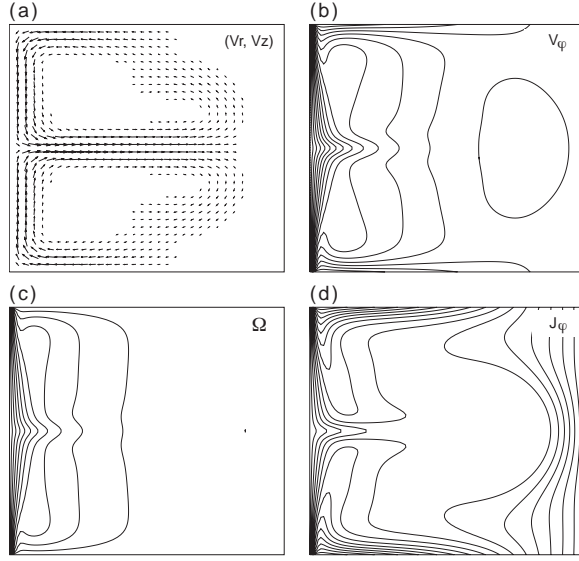
FIGURE 4. Flow under enforced symmetry about $z = 0$ for $Re = 1600$: (a) Poloidal flow denoted by vector arrows; (b) toroidal velocity v_φ; (c) angular velocity Ω; and (d) angular momentum $J = rv_\varphi$.

The experimental results are shown in Fig. 3 for the case of $\Omega_1/2\pi = 2000$ rpm and $\Omega_2/2\pi = 150$ rpm at $z = 4$cm. The measured velocity is significantly smaller than the values predicted in an infinitely long circular Couette flow. Without allowance for these qualitative deviations, the previous local and global stability analyses would be invalid. The actual flow, if magnetized, would be locally stable to MRI at larger radii [Region (III) in Fig. 1(b)] and unstable to hydrodynamic modes at small radii [Region (I) in Fig. 1(b)].

HYDRODYNAMIC SIMULATION

In order to understand the velocity profiles measured in water, a nonlinear hydrodynamic code has been written in two dimensions using realistic boundary conditions at the endcaps. The stream-vorticity method [24] in the cylindrical coordinates (r, φ, z) is used to ensure incompressibility. Time integration is performed by fourth-order Runge-Kutta on uniform poloidal grids at resolutions on the order of 100×100 and Reynolds numbers (Re) up to 3200. The code has been benchmarked at low Re where analytic solutions exist.

Fig. 4 shows the case $Re = 1600$. Ekman boundary layers form at both endcaps with increasing thickness towards the inner cylinder. The average thickness is on the order of $0.1h$, which is somewhat larger than the value $\delta_E \approx \sqrt{\nu/\bar{\Omega}} \sim .03h$ expected for uniform rotation, but is more consistent with estimates for the differentially rotating case [25]: $\delta_E \approx \sqrt{2\nu/\bar{\kappa}} \sim 0.085h$. Circulation occurs in two poloidal cells, their convergence
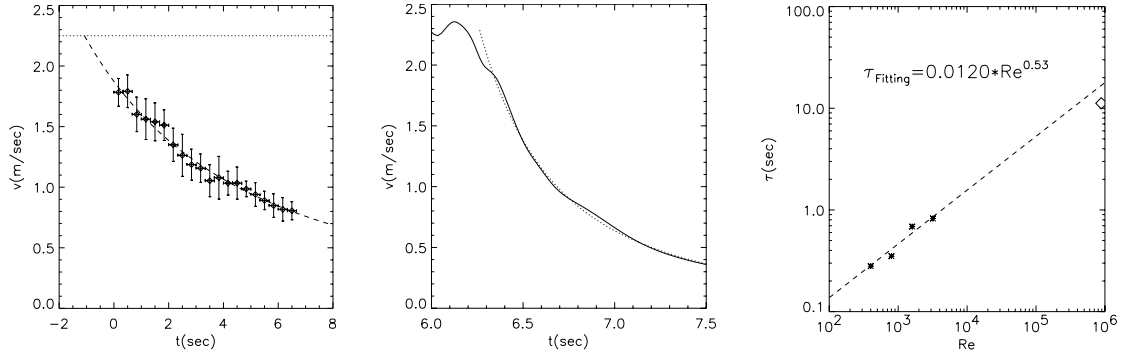
FIGURE 5. (left) Measured toroidal velocity at $r = 11.5 \pm 1$ cm and $z = 3 \pm 0.5$ cm during a spin down experiment. Dotted line is the toroidal velocity during steady state when inner and outer cylinders are rotated at $\Omega_1 = 2000$ rpm and $\Omega_2 = 150$ rpm, respectively. (center) Toroidal velocity averaged over the same volume in the simulation where the boundaries are stopped at $t = 6.0747$ second in the case of $Re = 3200$. (right) Spin down time versus Re for simulations (asterisks) and experiment (diamonds). Dotted line is a fit to the simulations only.

produces a jet-like feature, which is found to be unsteady at higher Re.

Although the peak poloidal flow is only a few percent of the toroidal , its effects on the toroidal flow are significant, as seen in Fig. 3. The angular velocity, Ω, is qualitatively different from the circular Couette flow (1). Most of the gradient in Ω concentrates near the inner cylinder, while the outer part is close to rigid body rotation. Simulated radial profiles of toroidal velocity are shown in Fig. 3 at $z = 4$cm for $Re = 1600$ and $Re = 3200$. These are in excellent agreement with the measurements, which is rather remarkable in view of the facts that the experimental Reynolds number is ~ 300 times larger than that of the simulations achieved in simulations and experiments, and that the simulations are performed in only two dimensions.

To further test the validity of our simulations, a series of experiments and simulations has been performed to study transient behavior of the system when both cylinders (and endcaps) are suddenly stopped. The rate of spin-down reflects the efficiency at which the Ekman circulation transports angular momentum. Experimentally, after a steady flow has been established, both cylinders are braked to a complete stop within about one second. The measured flow speed averaged over the annular volume $(r,z) \in (11.5 \pm 1, 3 \pm 0.5)$ cm is shown against time in Fig. 5(left).

We should not use a simple exponential fit to the measured data to find the spin down time, τ, because τ itself depends on velocity: $\tau = h/2\delta\bar{\kappa} = h/2\sqrt{\nu\bar{\kappa}}$, where the factor 2 comes from the fact that the circulation has two cells. Thus, assuming $\bar{\kappa} \propto \bar{\Omega}$, we have $d\bar{\Omega}/dt = -\bar{\Omega}/\tau \propto -\bar{\Omega}^{3/2}$, which leads to

$$\bar{\Omega}(t) = \frac{\bar{\Omega}(t_0)}{\left(1 + \frac{t-t_0}{\tau}\right)^2}. \tag{6}$$

The spin down time, $\tau = 11.2 \pm 0.9$ sec, is obtained by fitting Eq.(6) to the measurements as shown as dashed line in Fig. 5(left).
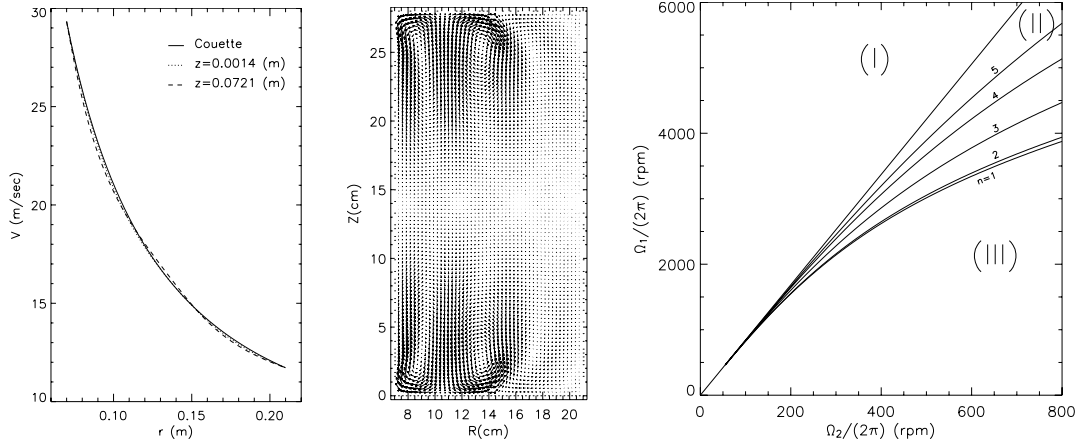
FIGURE 6. Simulated toroidal velocity profile (left) and poloidal flow (center) in a final optimized design using two rings at each end ($Re = 800$) and stability diagram in Ω_1 and Ω_2 space for the final design for each axial mode number based on local stability analysis (right).

A simulation of spin down at $Re = 3200$ is shown in Fig. 5(center). Again, τ is obtained by fitting Eq.(6). For the case of $Re = 3200$, $\tau = 0.82$ sec. Figure 5(right) displays τ as a function of Re and compares it to the best-fit power law, $\tau = 0.012 Re^{0.53}$ (dashed line). This power law agrees excellently with the simple estimate $\tau = H/2\sqrt{\nu \bar{\Omega}} \approx 0.011 Re^{1/2}$sec, and the experimental point is close to the extrapolation of the fit over two orders of magnitude in Re. The clear implication is that up to $Re \sim 10^6$, our flow is essentially laminar, although there is reason to believe that the boundary layer would become turbulent at slightly higher Re [25]. With the same boundary conditions, the gallium experiment might enter this turbulent regime since gallium has a lower kinematic viscosity ($\sim 0.2\times$), and the rotation rates will be somewhat higher. However, differentially rotating endcaps are likely to stabilize the boundary layer somewhat by reducing the velocity difference between the boundary and the neighboring interior flow.

GALLIUM EXPERIMENT

We have seen how the Ekman circulation transports angular momentum radially and significantly modifies the toroidal flow profile. Therefore it should be minimized in order to study MRI in a controlled fashion. One way to reduce the circulation is to divide the endcaps into multiple, differentially rotating rings. After an optimization process, it was found by simulation that two rings may suffice if they can rotate independently of the two cylinders. Figure 6(left) shows the simulated profile around the midplane for the case of $r_1 = 7$cm, $r_2 = 21$cm, $h = 28$cm, $\Omega_1/2\pi = 4000$rmp, and $\Omega_2/2\pi = 533$rpm. The angular velocity of the inner and outer rings are 1820rpm and 650rpm, respectively. The remaining Ekman cells are much more localized at each end [Fig.6(center)], and the resultant toroidal flow profile agrees excellently with the Couette solution (1), which for an appropriately chosen magnetic field should destabilize multiple axial MRI modes as shown in Fig. 6(right). The existence of multiple modes may allow mode-mode
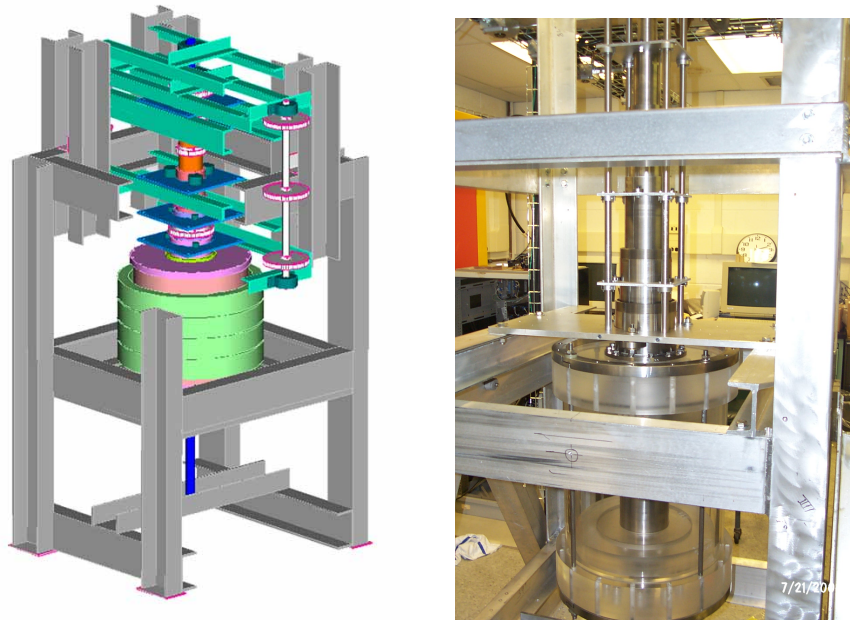
FIGURE 7. A 3D view of the gallium experiment (left) and a photograph of the nearly completed apparatus (right).

couplings, which may be important to the nonlinear behavior of MRI.

To implement the new design, substantial engineering efforts have been spent to accommodate multiple moving components with high mechanical stresses, while maintaining accurate balance and tight seals. The experimental apparatus (Fig. 7) consists of a containment vessel made of clear acrylic for the PIV measurements during a water test phase, four independently computer-controlled motors, and 6 magnets to provide a vertical magnetic field up to 0.8 Tesla with minimum redial component. Seven concentric stainless pipes along the central axis are used to drive both inner and outer cylinders and two pairs of rings at the ends. Each rotating component was accurately balanced separately (to minimize vibrations) and the apparatus has been successfully assembled. Currently, it is being tested with water, and should be ready for the MRI experiment with gallium in the near future. An extensive set of controls and diagnostics is being implemented to operate the experiment accurately and safely while providing quality data on torque couplings between rotating components, internal and external magnetic perturbations, internal pressure, and internal velocity. Fig. 7(right) shows a photograph of the nearly completed experimental apparatus.

Our first experimental step is to confirm the design by directly measuring the radial profile of toroidal flow in water, which may not be as smooth as as those of the relatively low-*Re* simulations shown in Fig.6(left). According to the Taylor-Proudman theorem, a steady rotating flow should be almost independent of height where viscosity is unimportant (*i.e.* outside boundary layers). Thus the velocity jumps at the edges of rings may extend well into the interior of the flow, forming what are known as Stewartson layers [26, 27]. Because of the small viscosity, however, the Stewartson layers may be unstable

[28], especially where angular momentum decreases outward across the layer. The addition of an axial magnetic field is expected to have no large influence on the structure of Stewartson layer [29], but may alter its stability.

The characteristic times of the gallium experiment are listed as follows: magnetic diffusion time $\tau_\eta <$10ms, Alfvén time $\tau_A = 25$ms at $B =$0.5T, MRI growth time $\tau_{MRI} \sim$50ms, $\tau_{spinup} \sim \tau_{Ekman} \geq 20$s, viscous time $\tau_\nu \sim 5000$ s. Based on these time scales, the following operational scenarios are planned.

1. A desired unmagnetized flow is set up by pre-programmed speeds for all four motors. This takes at least τ_{Ekman}.
2. An appropriate magnetic field is imposed to trigger MRI. The penetration time for the magnetic field, τ_η, is shorter than other relevant time scales. MRI is expected to grow on the time scale τ_{MRI}, and all diagnostics are expected to detect its existence.
3. Nonlinear saturation of MRI is expected to depend upon the initial flow profile and magnetic field strength. Such information is crucial to characterizing the efficiency of angular-momentum transport by MRI in the incompressible limit.
4. Additional external drives are possible by continuously changing the speeds of the end rings even after MRI starts to grow. The characteristic time for flow to change axially with a strong magnetic field is τ_A, which is comparable to τ_{MRI}. Enhanced nonlinear saturation in response to such additional drives is of great interests since they may lead to turbulence and new relaxation phenomena, as suggested by numerical simulations [30, 31].

Another physical issue concerns the effect of magnetic field on the residual Ekman circulation, which will possibly be the main competing mechanism for angular momentum transport in this experiment. Local linear theory [32, 33] predicts a transition from an Ekman layer thickness $\delta_E = \sqrt{\nu/\Omega}$ to a Hartmann layer thickness $\delta_H = \sqrt{\nu\eta}/V_A$ with increasing magnetic field. If the field is sufficiently large, this so-called Ekman-Hartmann layer shrinks, predicting a reduced Ekman circulation. Globally, however, the induced current [32] may reach deeper into bulk of the flow, depending on parameter regimes [34]. In addition, the Ekman-Hartmann layer is subject to instabilities [35], which may broaden its thickness, and thus increase the Ekman circulation. Experimentally, magnetic Ekman circulation can be studied by choosing specific operation parameters so that the flow is stable to both hydrodynamic modes and also to MRI when a magnetic field with appropriate strength is applied.

A number of numerical projects are underway to directly simulate the gallium experiment using realistic boundary conditions. One class of simulations uses incompressible MHD codes, either based on the existing 2D hydrodynamic code [25] or on a new method using spectral and finite element [36]. Another class uses existing compressible MHD codes, such as ZEUS [37, 38], which has been extensively used to simulate MRI in astrophysical accretion disks. Comparisons between results from experiment, and compressible and incompressible codes with realistic boundary conditions (but likely with unrealistic Reynolds numbers), under the guidance of theoretical analysis, should provide much needed insights of the underlying nonlinear physics of MRI, and its implications for astrophysics.

DISCUSSIONS AND CONCLUSIONS

Other potential mechanisms to transport angular momentum by hydrodynamic turbulence deserve some remarks here. Richard & Zahn [8, henceforth RZ] have argued that purely hydrodynamic turbulence may provide an effective viscosity

$$\nu_{\mathrm{T}} = -\beta r^3 \frac{\partial \Omega}{\partial r}\,, \qquad \beta \approx 1.5 \times 10^{-5}, \tag{7}$$

based on old Couette-flow experiments [39, 40] in which, at Reynolds numbers $Re^* \equiv r^3 \Delta\Omega / \nu \Delta r$ larger than $Re^*_{\mathrm{crit}} \approx 6 \times 10^5$, the flow became turbulent, even when the inner cylinder was at rest—a strongly Rayleigh-stable case. RZ attribute this to finite-amplitude instability and deduce a viscosity of the form (7) with $\beta = 1/Re^*_{\mathrm{crit}}$. If applicable to accretion disks, this is very important, especially for disks too weakly ionized for MRI. The form (7), however, is *nonlocal* because of its explicit dependence on radius, so local simulations would not find it. There have been few Couette-flow experiments relevant to RZ's hypothesis since those of Wendt and Taylor, which however have now been partially confirmed by [41]. In addition, the existing results on this subject have been limited to small gaps, i.e., $\Delta R/R \leq 1/3$, which is far from the situation in accretion disks. Our experiment will probe the relevant regime with a relatively larger gap $\Delta R/R \sim 1$, though we will need to pay attention to wall effects [42] that do not exist in accretion disks. By varying the magnetic field, we can also measure the *relative* importance of MRI and hydrodynamic instability in our apparatus. In addition, the effects of magnetic field on finite-amplitude hydrodynamic instability, if it does exist, can also be studied; this is of interest because even cold disks (*e.g.*, protostellar disks) may be partially ionized by nonthermal sources (X-rays, cosmic rays) and therefore somewhat magnetized. Since RZ, other finite-amplitude or even linear instabilities of Rayleigh-stable Couette flows of astrophysical relevance have been proposed[9, 43, 44, 45].

Here a few comments on the other related experiments are in order. A liquid sodium experiment in a similar Couette flow geometry is underway [46]. It will have larger magnetic Reynolds number and Lundquist number than ours, but will likely suffer from Ekman circulation, and consequently a poorly controlled background toroidal flow, since the end plates corotate with outer cylinder (as in our water-based prototype experiments).

Another experiment in spherical geometry has already claimed to see MRI [47]. Since the outer sphere does not rotate, however, this experiment should suffer hydrodynamic (centrifugal) instability even before the field is applied, as in Region I of Fig. 1. The observed lower threshold for non-axisymmetric modes is inconsistent with theoretical predictions on first excitation of axisymmetric modes [48]. Furthermore, possible other candidate instabilities, such as magnetized centrifugal and Kelvin-Helmholtz instabilities, were not discussed, nor the aforementioned magnetic Ekman effect. While the experiment does find enhanced angular-momentum transport associated with an applied poloidal field, it is not clear how the enhancement relates to MRI in disks. These complications stem from a design that was probably intended mainly to imitate planetary dynamos rather than MRI in accretion disks.

In summary, a brief review of an ongoing experimental project to study MRI in a short Couette flow of liquid gallium has been given. Interplay between experiment, simulation, and theory has been proven to be an effective approach to uncover the underlying physics being investigated. Theoretical insights provide crucial guidance for the experi-

ment while simulations bridge highly-idealized theoretical ideas to a more complicated real world. It was found that rapid Ekman circulation due to endcaps can effectively transport angular momentum, and thus qualitatively modify flow profiles. An optimized new apparatus has been designed and constructed. The engineering for this unique device was challenging but surmountable. In addition to MRI, a few related important physics issues can also be studied using the same apparatus, including existence and stability of Stewartson layer, magnetic Ekman circulation, and nonlinear hydrodynamic instabilities. Our intention is to minimize all these complications in order to clearly demonstrate MRI and study its nonlinear effects in detail.

ACKNOWLEDGMENTS

REFERENCES

1. Velikhov, E. P., *Sov. Phys. JETP*, **36**, 995–998 (1959).
2. Chandrasekhar, S., *Proc. Nat. Acad. Sci.*, **46**, 253–257 (1960).
3. Balbus, S., and Hawley, J., *Astrophys. J.*, **376**, 214–222 (1991).
4. Hawley, J. F., Gammie, C. F., and Balbus, S. A., *Astrophys. J.*, **470**, 742–763 (1995).
5. Brandenburg, A., Nordlund, A., Stein, R. F., and Torkelson, U., *Astrophys. J.*, **446**, 741–754 (1995).
6. Matsumoto, R., and Tajima, T., *Astrophys. J.*, **445**, 767–779 (1995).
7. Balbus, S., and Hawley, J., *Rev. Mod. Phys.*, **70**, 1–53 (1998).
8. Richard, D., and Zahn, J.-P., *Astron. Astrophys.*, **347**, 734–738 (1999).
9. Huré, J.-M., Richard, D., and Zahn, J.-P., *Astron. Astrophys.*, **367**, 1087–1094 (2001).
10. Ji, H., Goodman, J., and Kageyama, A., *Mon. Not. Astron. Soc.*, **325**, L1–L5 (2001).
11. Goodman, J., and Ji, H., *J. Fluid Mech.*, **462**, 365 (2002).
12. Donnelly, R. J., and Ozima, M., *Phys. Rev. Lett.*, **4**, 497–498 (1960).
13. Donnelly, R. J., and Ozima, M., *Proc. R. Soc. Lond. A*, **266**, 272–286 (1962).
14. Donnelly, R. J., and Caldwell, D. R., *J. Fluid Mech.*, **19**, 257–263 (1964).
15. Brahme, A., *Physica Scripta*, **2**, 108–112 (1970).
16. Rüdiger, G., and Zhang, Y., *Astron. Astrophys.*, **378**, 302–308 (2001).
17. Willis, A. P., and Barenghi, C. F., *Astron. Astrophys.*, **388**, 688–691 (2002).
18. Rüdiger, G., and Shalybkov, D., *Phys. Rev. E*, **66**, 16307 (2002).
19. Rüdiger, G., Schultz, M., and Shalybkov, D., *Phys. Rev. E*, **67**, 46312 (2003).
20. Sano, T., and Miyama, S., *ApJ*, **515**, 776 (1999).
21. Chandrasekhar, S., *Hydrodynamic and Hydromagnetic Stability.*, Oxford University Press., 1961.
22. Herron, I., and Goodman, J., Why the small-P_m approximation suppresses the MRI. (2004), in preparation.
23. Raffel, M., Willert, C., and Kompenhans, J., *Particle Image Velocimetry: A Practical Guide.*, Springer, 1998.
24. Ferziger, J. H., and Peric, M., *Computational Methods for Fluid Dynamics*, Springer, 2002, 3rd edn.
25. Kageyama, A., Ji, H., Goodman, J., Chen, F., and Shoshan, E., *to appear in J. Phys. Soc. Jpn.*, **73** (2004).
26. Stewartson, K., *J. Fluid Mech.*, **3**, 17 (1957).
27. Rüdiger, G., and Hollerbach, R., *The Magnetic Universe*, Wiley-VCH Verlag GmbH & Co., 2004.
28. Hollerbach, R., *J. Fluid Mech.*, **492**, 289 (2003).
29. Ingham, D., *Phys. Fluids*, **12**, 389–396 (1969).
30. Fleming, T., Stone, J., and Hawley, J., *Astrophys. J.*, **530**, 464–477 (2000).

31. Sano, T., and Inutsuka, S., *Astrophys. J.*, **561**, L179–L182 (2001).
32. Gilman, P., and Benton, E., *Phys. Fluids*, **11**, 2397 (1968).
33. Pariev, V. I., *Magnetohydrodynamics*, **39**, 123–146 (2003).
34. Vempaty, S., and Loper, D., *Phys. Fluids*, **12**, 1678–1686 (1975).
35. Gilman, P., *Phys. Fluids*, **14**, 7 (1971).
36. Cattaneo, F., Obabka, A., and Fischer, P. (2004), private communication.
37. Stone, J. M., and Norman, M. L., *Astrophys. J. Suppl.*, **80**, 753–790 (1992).
38. Stone, J. M., and Norman, M. L., *Astrophys. J. Suppl.*, **80**, 791–818 (1992).
39. Wendt, F., *Ing. Arch.*, **4**, 577 (1933).
40. Taylor, G., *Proc. Roy. Soc. London A*, **157**, 546 (1936).
41. Richard, D., *Instabilités Hydrodynamiques dans les Ecoulements en Rotation Différentielle*, Ph.D. thesis, Université Paris 7 (2001).
42. Schultz-Grunow, F., *Z. angew. Math. Mech.*, **39**, 101 (1959).
43. Molemaker, M. J., McWilliams, J. C., and Yavneh, I., *Phys. Rev. Lett.*, **86** (2001).
44. Longaretti, P., *Astrophys. J.*, **576**, 587–598 (2002).
45. Chagelishvili, G. D., Zahn, J.-P., Tevzadze, A. G., and Lominadze, J. G., *Astron. Astrophys.*, **402**, 401–407 (2003).
46. Noguchi, K., Pariev, V. I., Colgate, S. A., Beckley, H. F., and Nordhaus, J., *Astrophys. J.*, **575**, 1151–1162 (2002).
47. Sisan, D., Mujica, N., Tillotson, W., Huang, Y.-M., Dorland, W., Hassam, A., Antonsen, T., and Lathrop, D., First experimental observation and characterization of the magnetorotational instability (2004), `arXiv:physics/0402125`.
48. Kitchatinov, L., and Rüdiger, G., *Mon. Not. R. Astron. Soc.*, **286**, 757–764 (1997).